APPLIED PHYSICS

Mitigating cavitation erosion using biomimetic gas-entrapping microtextured surfaces (GEMS)

Silvestre Roberto Gonzalez-Avila[1]*†‡, Dang Minh Nguyen[1,2]*, Sankara Arunachalam[3], Eddy M. Domingues[3], Himanshu Mishra[3‡], Claus-Dieter Ohl[1,2]

Cavitation refers to the formation and collapse of vapor bubbles near solid boundaries in high-speed flows, such as ship propellers and pumps. During this process, cavitation bubbles focus fluid energy on the solid surface by forming high-speed jets, leading to damage and downtime of machinery. In response, numerous surface treatments to counteract this effect have been explored, including perfluorinated coatings and surface hardening, but they all succumb to cavitation erosion eventually. Here, we report on biomimetic gas-entrapping microtextured surfaces (GEMS) that robustly entrap air when immersed in water regardless of the wetting nature of the substrate. Crucially, the entrapment of air inside the cavities repels cavitation bubbles away from the surface, thereby preventing cavitation damage. We provide mechanistic insights by treating the system as a potential flow problem of a multi-bubble system. Our findings present a possible avenue for mitigating cavitation erosion through the application of inexpensive and environmentally friendly materials.

INTRODUCTION

A wide variety of small- and large-scale processes involves the interaction of solids and liquids when one or both of these media are in motion, often at high speeds. Examples include pumps, such as those used by thermoelectric power generation, to transfer water over long distances, control valves, propellers, and impellers, which are used widely in marine transportation (*1*–*3*). These processes often result in the formation of vapor bubbles—a phenomenon known as cavitation (*1*, *2*). These transient cavitation bubbles subsequently implode, creating pressure waves and liquid jets directed toward the solid interface at speeds of the order 80 m s^{-1}. This causes undesirable noise, mechanical vibrations, surface erosion, and reduced energy efficiency (*1*, *2*, *4*). Cavitation bubbles can also result from the localized heating of liquids, such as in spallation neutron source facilities, damaging operational targets (*5*, *6*). Because of the high costs associated with a reduction in energy efficiency, and the repair and downtime of damaged equipment, a number of strategies for mitigating cavitation erosion have been explored. These include the structural optimization of hydrodynamic equipment (*3*, *7*), the development of stronger materials and coatings (*8*, *9*), boronizing, laser surface hardening, cladding, and chemical and physical vapor deposition, which is reviewed in (*10*). However, all these approaches ultimately fail to prevent cavitation erosion in the long term, and thus, new mitigation strategies are desirable.

On the one hand, cavitation bubbles that collapse near a liquid-solid interface are accelerated toward and forcefully affect the interface with a high-speed jet (*2*). On the other hand, cavitation bubbles that collapse near a free boundary, such as a liquid-vapor interface, are repelled away from it (*11*). However, the latter observation at liquid-vapor interfaces has not been adequately explored for the rational design of cavitation-free surfaces. Most designs use perfluorinated coatings to trap air at the solid-water interface, but their vulnerability to abrasion (*12*), high mechanical (*13*) and thermal stresses (*14*) during engineering flows, and contamination (*15*), along with their environmental impact (*16*), have limited their wide-scale application. Thus, alternative approaches for entrapping air at the solid-liquid interface that avoid the use of chemical coatings are preferable, and they could bring a paradigm shift in the design and development of materials and processes for mitigating cavitation damage.

In this work, we describe a biomimetic approach to trap air at the solid-liquid interface without using coatings and demonstrate the efficacy of this approach at repelling cavitation bubbles. We draw inspiration from the natural world: Springtails (*Collembola*) (*17*) and sea skaters (*Halobates germanus*) (*18*) are two unrelated insects that live in soils and the open ocean, respectively, and both have evolved particular strategies to repel water. Specifically, the cuticles of springtails and the body hairs of sea skaters are composed of granules (*19*) and microtrichia (*20*), respectively, which have mushroom-shaped features that robustly trap air for breathing and buoyancy when the insect is accidentally submerged in water (Fig. 1).

Inspired by these insects, researchers have demonstrated that by carving mushroom-shaped microtexture pillars (*21*–*23*) and microcavities (*17*, *24*–*28*) on surfaces, even intrinsically wetting surfaces can trap air when immersed in liquids. While the inherent wettability of materials dictates that the fully filled or the "Wenzel" state (*29*) should be the thermodynamic minima, air-filled or metastable "Cassie" states (*30*) can be engineered to persist for longer durations (*31*). For instance, Mishra *et al.* (*32*) have recently demonstrated that the air trapped inside silica surfaces with mushroom-shaped cavities immersed in hexadecane (intrinsic contact angle on smooth SiO_2 in air, $\theta_o = 20°$) remains intact over 100 million times longer time span as compared to simple cylindrical cavities, although the solid, liquid, and vapor phases are chemically identical. On immersion in a wetting liquid, the mushroom-shaped features can stabilize the

[1]Department for Soft Matter, Institute for Physics, Otto-von-Guerick University, 39106 Magdeburg, Germany. [2]School of Physical and Mathematical Sciences, Department of Physics and Applied Physics, Nanyang Technological University, Singapore 637371, Singapore. [3]King Abdullah University of Science and Technology (KAUST), Water Desalination and Reuse Center (WDRC), Biological and Environmental Science and Engineering (BESE) Division, Thuwal 23955-6900, Saudi Arabia.
*These authors contributed equally to this work.
†Present address: University of Poitiers—École Nationale Supérieure de Mécanique et d'Aérotechnique (ENSMA) Téléport 2, 1 Avenue Clément Ader, 86360 Chasseneuil-du-Poitou, France.
‡Corresponding author. Email: roberto_glez83@hotmail.com (S.R.G.-A.); himanshu.mishra@kaust.edu.sa (H.M.)

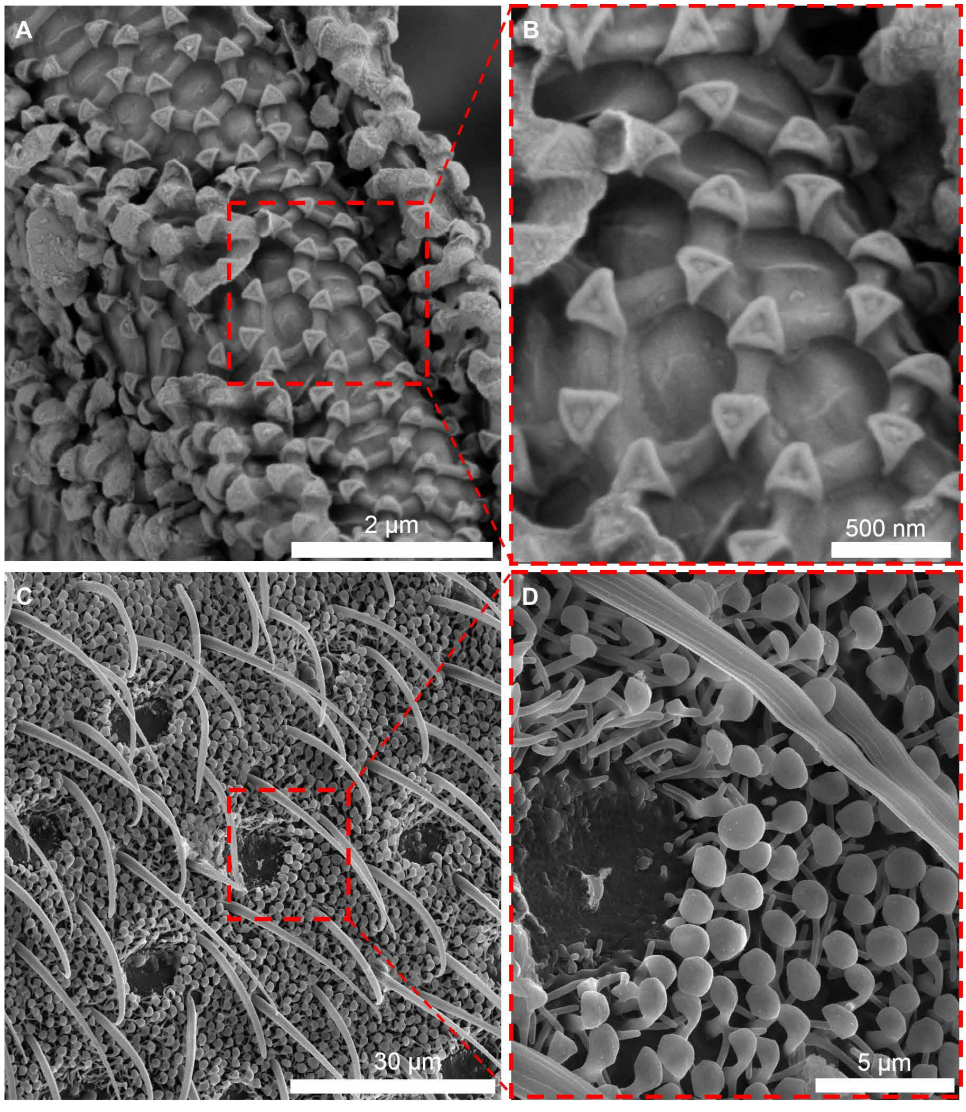

Fig. 1. Representative scanning electron micrographs of cuticles and fine hairs on the mesothorax of springtails (*Collembola*) and sea skaters (*H. germanus*), respectively. (**A** and **B**) Springtails have primary granules (triangular) connected by ridges forming honeycomb patterns that prevent the intrusion of liquids on submersion. (**C**) Long needle-shaped hairs and tiny mushroom-shaped hairs on dorsal and ventral mesothorax of sea skaters provide robust repellency against seawater. (**D**) Magnified micrograph of mushroom-shaped hairs. Photo credit: Sankara Arunachalam, KAUST.

intruding liquid meniscus and entrap air. This result underscores the efficacy of mushroom-shaped microtextures at entrapping air on immersion in liquids (without relying on chemical coatings). Researchers have also compared the time dependence of wetting transitions of liquids on silica surfaces with arrays of mushroom-shaped pillars and cavities, providing insights into the optimal geometrical parameters for designing gas-entrapping microtextured surfaces (GEMS) (*24*, *32*, *33*). On the basis of those insights and our previous work on cavitation (*34*–*36*), here, we consider that the air inside GEMS might present a durable "free" boundary to cavitation bubbles, leading to a coating-free strategy for mitigating cavitation erosion. We demonstrate the feasibility and efficacy of this approach by comparing the fates of laser-produced cavitation bubbles generated at precisely controlled distances from silica-GEMS and smooth silica surfaces (Fig. 2). We also explain the behaviors of these bubbles using a simple potential flow model.

RESULTS

The fabrication of the GEMS structure

We fabricated arrays of circular microcavities containing mushroom-shaped inlets in a hexagonal lattice on SiO_2/Si surfaces ($\theta_o = 40° \pm 2°$ for the air/water system), which we refer to as silica-GEMS (Fig. 3, A to D, and section S1). This spatial arrangement maximizes the liquid-vapor surface area, the free boundary perceived by the cavitation bubbles. We compare the performance of silica-GEMS containing arrays of microcavities with diameters $D = 50$ and 200 μm, separated by an inter-cavity distance $L = D + 12$ μm (fig. S3 and table S1). To compare the performance of our coating-free approach with a coating-based approach, we grafted perfluorodecyltrichlorosilane (FDTS; $\theta_o = 113° \pm 1°$ for the air/water system) onto silica-GEMS by molecular vapor deposition (MVD; details in section S2).

When drops of water ($V \approx 2$ μl) are placed on the silica-GEMS and advanced and retracted at the rate of 0.2 μl s^{-1}, the apparent

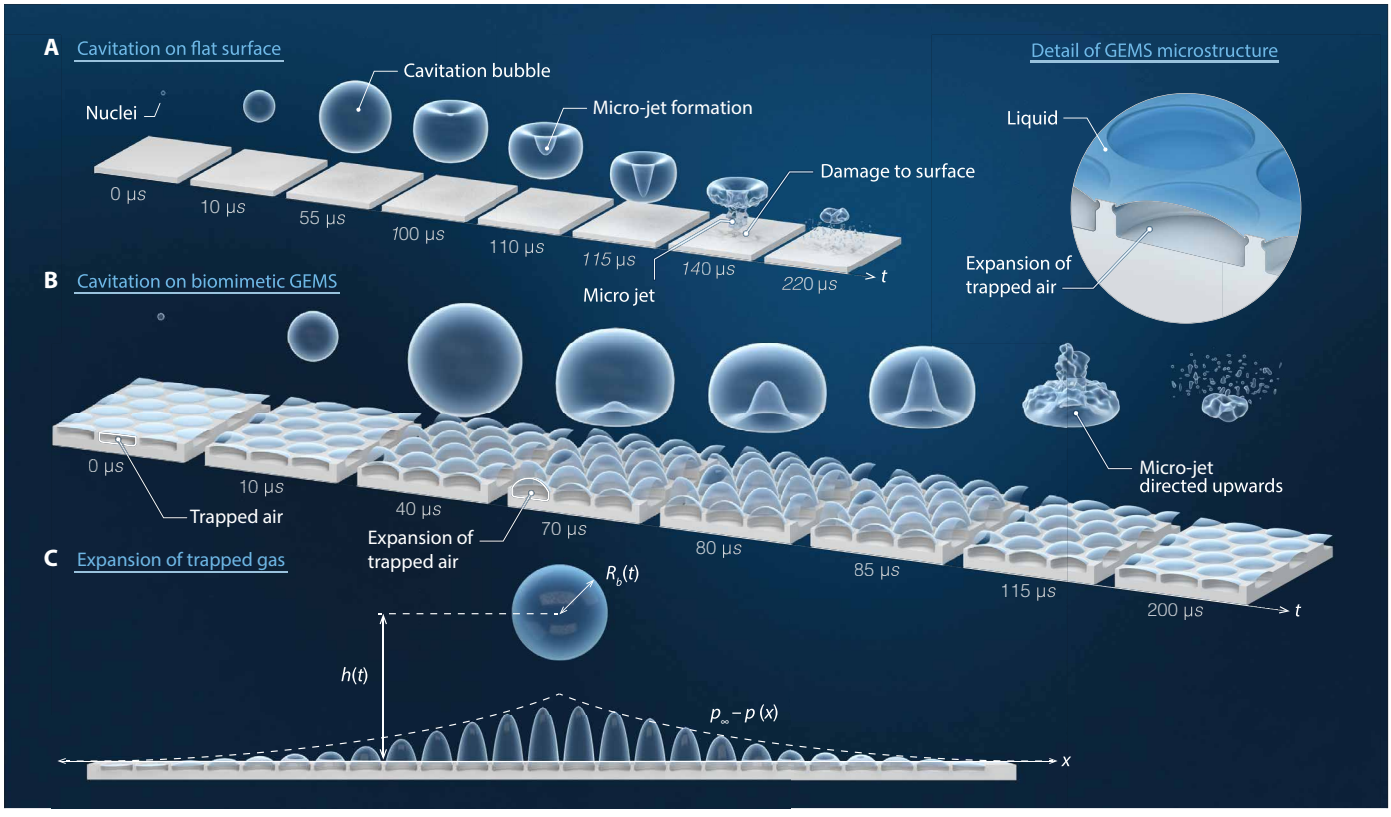

Fig. 2. Illustration summarizing how GEMS prevent damage from cavitation jets. (**A**) Liquid jet from a bubble collapsing close to a solid boundary affecting the substrate and causing erosion. The time scale corresponds to a cavitation bubble of $R_{max} \approx 570$ μm. (**B**) The gas entrapped inside the GEMS protrudes near the cavitation bubble and behaves as a free boundary. As a result, the liquid jet from the collapsing bubble is directed away from the substrate. The time scale shown is that of a cavitation bubble of $R_{max} \approx 520$ μm. The time in μs and maximum bubble radius depicted in (A) and (B) are typical values observed in the experiments. (**C**) The gas entrapped inside the GEMS expands because of the pressure field generated by the nearby cavitation bubble. Notice that the gas contained in the GEMS bulges outward and reaches an almost hemispherical shape during the expansion of the cavitation bubble as mentioned in the text. Image credit: Xavier Pita, Scientific Illustrator, KAUST.

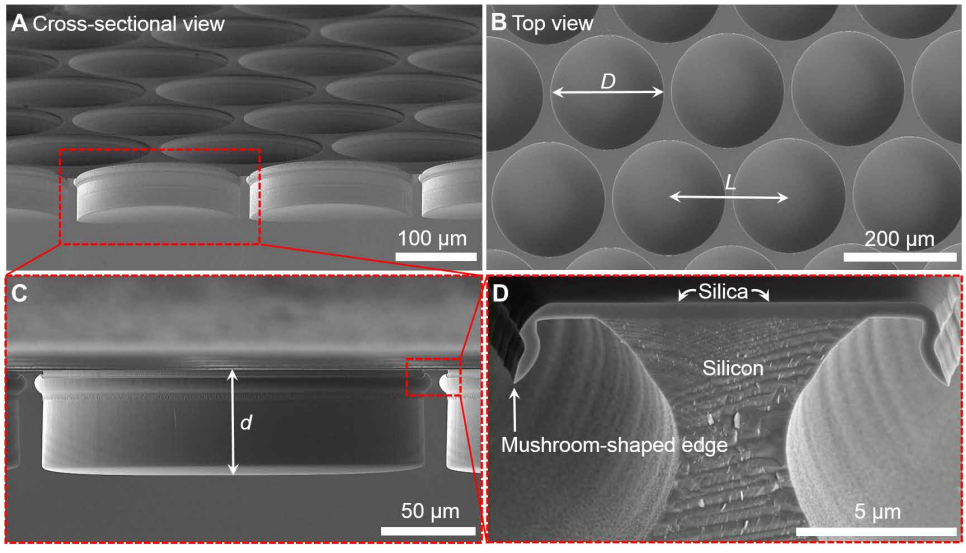

Fig. 3. Scanning electron micrographs of silica-GEMS. (**A**) Tilted cross-sectional view (35°) of the silica-GEMS. (**B**) Top view of the silica-GEMS comprising circular cavities in a hexagonal distribution. (**C**) Cross-sectional view of the single cavity shown in (A). (**D**) Detailed cross-sectional view of the mushroom-shaped edge. This sharp edge stabilizes the intruding liquid meniscus and facilitates the entrapment of air inside the cavity. Photo credit: Sankara Arunachalam, KAUST.

contact angles are found to be $\theta_r > 100°$ (Fig. 4, A and B, and table S2). Because the volume of the entrapped gas inside the GEMS microcavities is much smaller than the water droplets, i.e., they are well below the capillary length of water (*37*), we can apply the Cassie-Baxter model (*30*) to predict apparent contact angles (section S3). We find a reasonable agreement between the predictions of the apparent contact angles, θ_{Pr}, and the experimental data (table S2). The receding contact angles of water on silica-GEMS are $\theta_R \approx 0°$ due to the interconnected nature of the microtexture (*24*, *38*), leading to the formation of liquid bridges during receding (*39*). The receding contact angles on FDTS-coated GEMS are $\theta_R \approx 100°$ due to lower adhesion/pinning forces. On immersion in water, silica-GEMS trap air inside the mushroom-shaped microcavities (fig. S4). We use confocal laser scanning microscopy (fig. S5; see Materials and Methods) to visualize the liquid-vapor interface (Fig. 4C). Because of the capillary condensation of water inside hydrophilic silica-GEMS, the displaced air pushes the liquid-vapor interface upward (Fig. 4D; cross-sectional view). However, FDTS-coated GEMS experience much lower capillary condensation under ambient conditions (293 K, 1 atm).

The interactions between cavitation bubbles and GEMS

To measure the impact of cavitation events on the silica-GEMS systematically, we use a pulsed laser system to locally vaporize water and create cavitation bubbles at precisely controlled distances, h, from solid surfaces as seen in section S4. We introduce a nondimensional standoff parameter, $\gamma = h/R_{max}$, where R_{max} is the maximum bubble radius and h is the distance between the point of inception of the bubble and the surface; γ describes the overall bubble dynamics in the experiments and computer simulations (fig. S6) (*40*). We investigated the response of the entrapped gas in GEMS to cavitation bubbles in the range $5.1 > \gamma > 0.7$.

Figure 5 compares the dynamics of cavitation bubbles created close to a smooth silica surface (Fig. 5A and movie S1) and silica-GEMS (Fig. 5B and movie S2). Figure 5A depicts selected frames of representative bubble dynamics near a smooth silica surface—a bare rigid boundary located at the bottom in Fig. 5A—for $\gamma = 4.8$ and bubble radius, $R_{max} = 630$ μm. The bubble expands to a maximum radial size at $t = 60$ μs and collapses around $t = 120$ μs; during collapse, the bubble moves toward the silica surface, forming a liquid jet that could potentially damage the surface. In contrast, the cavitation bubble produced next to the silica-GEMS has distinct dynamics. As shown in Fig. 5B, this cavitation bubble expands and collapses ($R_{max} = 610$ μm, $\gamma = 5.1$) similarly to Fig. 5A, but unlike the smooth silica surface, the resulting bubble jet moves away from the surface, as evidenced by the upward motion of the centroid (Fig. 5B). The expansion of the trapped gas in silica-GEMS is indicated by the arrow in the first frame of Fig. 5B and the top-view images in Fig. 5C (movie S3). During the early stages of the bubble expansion, $t = 25$ μs, the trapped gas in the cavities bulges outward and reaches an almost hemispherical shape at $t = 50$ μs, but when the bubble collapses, the trapped gas in the silica-GEMS shrinks and returns to normal. We verify the reproducibility of our observations by recording identical bubble dynamics for up to 30 laser-created bubbles, i.e., the created cavitation bubbles were all equally repelled by the silica-GEMS surface. Cavitation bubble dynamics close to the silica-GEMS are similar to those of silica-GEMS coated with FDTS (section S5, fig. S7, and movies S4 and S5), underscoring the efficacy of our coating-free biomimetic strategy.

Next, we investigate the robustness of the silica-GEMS at mitigating cavitation erosion for bubbles that collapse closer to the microtextured surface than the previous examples. The internal pressure of the trapped air in the silica-GEMS during expansion and shrinkage is approximately equal to the vapor pressure. We found that the stability of the trapped air is dependent on the distance of the collapsing bubble from the surface, i.e., the trapped air can only recover if the cavitation bubble collapses at sufficiently large distances from the surface. Because of the close distances between microcavities, the trapped gas experiences a reduction in pressure when a cavitation bubble collapses nearby, causing the trapped gas to expand. By producing cavitation bubbles closer to the silica-GEMS, such as at $\gamma = 1.8$ and $R_{max} = 530$ μm, for example, we expose the microcavities to even lower pressures, as portrayed in Fig. 6A (fig. S8A and movies

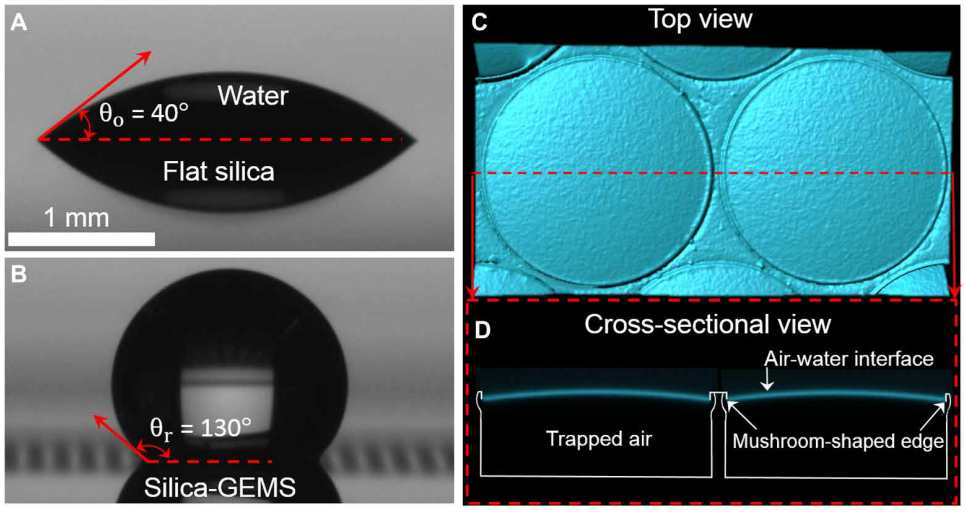

Fig. 4. Comparison of wetting behaviors of smooth silica and silica-GEMS with water. (**A**) Smooth silica surfaces are water-wet, characterized by intrinsic contact angles, $\theta_o < 90°$. (**B**) Silica-GEMS robustly entrap air underwater and show apparent contact angles, $\theta_r > 90°$. (**C** and **D**) Three-dimensional reconstructions of the air-water interface at the inlets of silica-GEMS underwater realized using confocal laser scanning microscopy. The cross-sectional view in (D) is along the dotted red line in (C). Scale bars are the same in (A) and (B), and the diameter of the cavities in (C) and (D) is $D = 200$ μm. Photo credit: Sankara Arunachalam, KAUST.

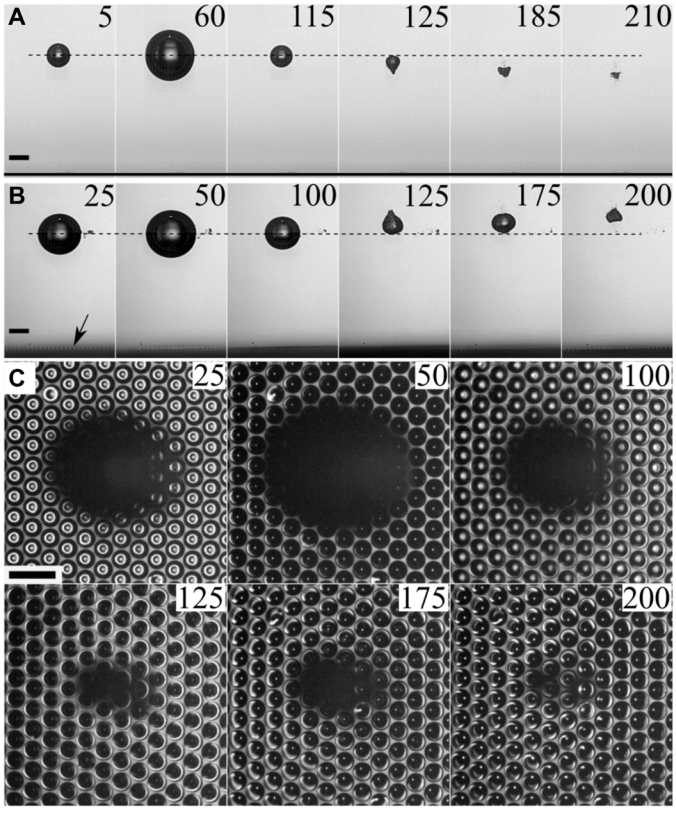

Fig. 5. Cavitation bubble dynamics at high standoff parameters. (**A**) Side view of the bubble near a smooth silica surface, $\gamma = 4.8$ and $R_{max} = 630$ μm. The bottom black line indicates the location of the surface. (**B**) Side view for the silica-GEMS, $\gamma = 5.1$ and $R_{max} = 610$ μm. The arrow indicates the location of the microcavities. (**C**) Top view of the microcavities portrayed in (B). Scale bar, 500 μm. The numbers on all the panels refer to time in microseconds after cavitation generation. The dotted lines in (A) and (B) serve to guide the eye for the direction of the jet after the bubbles collapse. These figures are derived from movies S1 to S3. Photo credit: Silvestre Roberto Gonzalez-Avila, OVGU.

S6 and S7). Under these conditions, the bubble collapses between $t = 85$ μs and $t = 90$ μs in a similar fashion to Fig. 5B (*41*), whereby the bubble centroid moves away from the surface. However, some of the gas trapped in the silica-GEMS escapes out of the cavities, forming smaller gas bubbles above the surface (Fig. 6A). At distances even closer to the boundary ($\gamma = 0.7$ and $R_{max} = 430$ μm), a critical point is reached where the cavitation bubble eventually coalesces with the trapped gas from the silica-GEMS (Fig. 6B, fig. S8B, and movies S8 and S9) and the system is no longer functional. With this gain of gas, the collapse of the cavitation bubble takes place much later, at $t = 130$ μs. In contrast, for the smooth silica surface, the bubble of similar size collapses at ≈80 μs (*42*). This effect is a result of the reduced impact velocity of ≈10 m s^{-1} of the bubble toward the GEMS, which is substantially lower than the value of ≈80 m s^{-1} for a solid silica surface (*4*).

We find that when cavitation bubbles are produced very close to silica-GEMS, the trapped air in the microcavities can be partially or fully expelled because of the expansion of the trapped gas during the bubble formation, the coalescence of entrapped gas in adjacent cavities as the bubble grows, and the depinning of the contact line from the mushroom-shaped edges. As a result, cavities get fully filled with water or get "deactivated" and can no longer repel cavitation jets. Along this theme, researchers have investigated cavitation in water on FDTS-coated nanoscale cavities in silicon (*43*) and on glass surfaces with a single cavity (*44*) and characterized surface damage during and after the collapse phase of the cavitation bubble as a function of the crystal structure of monocrystalline silicon (*45*). In all those scenarios, they found that the cavities got fully filled after the first cavitation event itself. In contrast, our bioinspired silica-GEMS are able to withstand 30 nucleation events after they get fully filled with water (fig. S9 and movie S10 show gas bubbles inside the microcavities after five cavitation events). Arguably, the remaining entrapped gas within our microcavities can also produce liquid jet in the following cavitation events, which can potentially damage the GEMS surface and contribute to the deactivation of the cavity, as reported in these studies. Here, our imaging system does not allow us to capture this mechanism, but we did not observe any damage to the GEMS surface after as many as 30 cavitation events. Once the microcavities are deactivated, the experiment can only be repeated if the substrate is taken of the liquid, dried, and resubmerged. These findings are consistent across coating-free silica-GEMS and FDTS-coated silica-GEMS.

It should be noted that even in the presence of tiny dirt particles, the functionality of silica-GEMS is not compromised. For instance, movie S5 captured a scenario with dirt particles attached to the microcavities. Yet, silica-GEMS entrapped air robustly and directed bubble jets away from the surface in every cavitation event (up to 27 tested attempts), and the surface remained undamaged. These findings underscore the efficacy of this approach in real-world scenarios.

Potential flow model

To gain insight into the physical mechanisms underpinning our experimental observations, we apply a simplified model through a numerical simulation, accounting for Bjerknes force and hydrodynamic drag (section S5) (*46*). Here, the trapped gas in the silica-GEMS is modeled using hexagonally arranged spherical bubbles, with their centers located at the centers of the cavities. The interaction of the cavitation bubbles with the trapped gas and the surface is modeled using an ideal flow model. Although this potential flow model neglects viscosity and pinning, it proves sufficient to describe the bubble dynamics on patterned surfaces (*34*). The present geometry with a cavitation bubble at a distance s from a substrate results in $N + 2$ spherical potential source terms, where N is the number of microcavities on the substrate. The two remaining sources are the laser-induced cavitation bubble and its mirror image, which accounts for the solid substrate. The translational motion of the cavitation bubble and its image is modeled with a force balance approach using Newton's second law

$$\frac{d}{dt}(M_i \mathbf{v_i}) = \frac{d}{dt}\left(\frac{1}{2}\rho V_i \mathbf{v_i}\right) = \mathbf{F}_{B,i} + \mathbf{F}_{D,i} \quad (1)$$

where i denotes the bubble under consideration, M_i is the bubble's virtual mass, $V_i = 4/3\pi R_i^3$ is the volume of the bubble, $\mathbf{F}_{B,i}$ is the secondary Bjerknes force, and $\mathbf{F}_{D,i}$ is the drag force (*46*).

The radial bubble dynamics are calculated using the Keller-Miksis model with an additional pressure term p_i resulting from the interaction between the main cavitation bubble and the entrapped gas (see Eq. 2) (*35*). Because the entrapped gas resides within the cavities, a solid layer separates them from each other, and thus, we can ignore their mutual pressure interaction. To simplify the calculation,

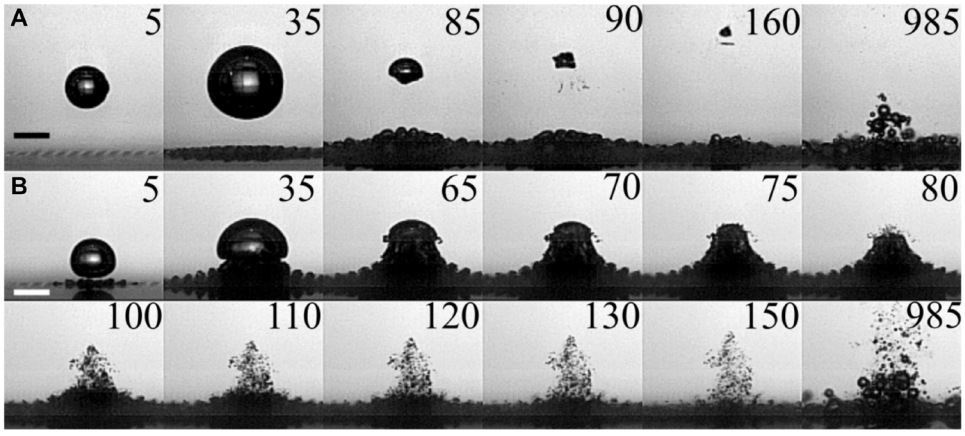

Fig. 6. Cavitation bubble dynamics on silica-GEMS at low standoff parameters. (**A**) Bubble dynamics for $\gamma = 1.8$ and $R_{max} = 530$ μm. (**B**) Bubble dynamics for $\gamma = 0.7$ and $R_{max} = 430$ μm. Scale bars, 500 μm. The numbers on all the panels refer to time in microseconds after the generation of the cavitation bubble. These figures are derived from movies S4 to S5. Bubble dynamics on perfluorinated silica-GEMS for similar γ values can be seen in fig. S8 and movies S7 and S9. Photo credit: Silvestre Roberto Gonzalez-Avila, OVGU.

all coalescence events are omitted, and the bubbles are allowed to overlap (section S6).

Figure 7A compares the simulation with the experimental observations from Fig. 6A for $\gamma = 1.8$. In the simulation, the cavitation bubble expands to a radius of $R_{max} = 525$ μm and collapses at $t = 90$ μs. The bubble radius development is well reproduced in Fig. 7B, in particular the asymmetry of the curve with a shorter expansion and a longer collapse phase. This asymmetry is likely caused by the growth of the entrapped gas in the GEMS, thereby effectively reducing the pressure and delaying the collapse of the cavitation bubble. Although the expansion of the trapped gas is qualitatively in agreement, their size is overestimated in the simulation and underestimated in duration, e.g., at $t = 50$ μs and $t = 85$ μs, respectively, in Fig. 7A. We attribute this difference to the fact that coalescence is neglected in our calculation. Coalescence could replace multiple small gas bubbles with a bubbling layer of larger effective radius, thus giving smaller curvature and therefore a longer collapsing time. However, the model does capture the behavior of the bubble moving away from the substrate, with the final displacement being approximately 250 μm, as shown Fig. 7B.

We perform a second simulation using a smooth substrate, i.e., with no trapped gas, and the same initial conditions of the cavitation bubble (and its image bubble) to compare with the silica-GEMS (Fig. 7C). Our calculations show that for smooth surfaces, cavitation bubbles grow considerably larger and move toward the surface, in contrast to silica-GEMS. Thus, silica-GEMS can mitigate cavitation erosion in two ways. First, the size of the cavitation bubble is reduced because the trapped gas consumes some of the fluid energy. Second, the silica-GEMS surface repels the cavitation bubble. While the present model is valid for sufficiently large distances between the cavitation bubble and the surface ($\gamma > 1$), it is not suitable for shorter distances such as shown in Fig. 6B.

To explain why the trapped gas in the silica-GEMS expands in the presence of a cavitation bubble, we explore the pressure generated by cavitation bubbles when they expand and shrink near a solid boundary. The pressure far from the bubble, p_∞, is assumed to be constant, i.e., atmospheric pressure. Again, we use a potential flow model (ignoring viscosity, the bubble content, and compressibility of liquid) accompanied with the method of images. We obtain the time and spatially dependent pressure $p(r,t)$ from Rayleigh's seminal work (*47*), which demonstrated that for most of the time, the pressure in the liquid and close to the bubbles is smaller than the far-field pressure. Figure 7D depicts the radial bubble dynamics for nine selected times, from t_0 to t_8. The pressure $p(x,t)$ is the pressure on the surface, with x being the radial coordinate. In this example, the bubble obtains a maximum radius of $R_{max} = 600$ μm for a distance of $\gamma = 3.0$. The symmetry of the potential flow solution results in an identical pressure distribution at the time of maximum radius, R_{max}, i.e., when there is no flow. During the early expansion ($t = t_0$), the pressure is maximum close to the bubble; thus, the pressure on the surface is higher than p_∞, while for $t = t_1$ and $t < t_7$, the pressure is monotonically reduced from the maximum at infinity. Figure 7E depicts the pressure $p(x,t_i)$ for $i = 0,...,8$ along the surface. At maximum expansion t_4, the stagnation point ($x = 0$) on the surface is exposed to a pressure of $p \approx 0.4$ bar. The trapped air embedded in the silica-GEMS initially forms a stable interface at pressure p_∞. As the pressure drops for $t > t_0$, the trapped air expands and covers the substrate, converting the rigid surface into a free interface. The pressure increases when the cavitation bubble collapses, but the inertia of the liquid delays the shrinkage and retreat of the trapped air. This slight delay allows the cavitation bubble to collapse, while the gas layer still covers the surface, protecting the silica-GEMS from the jet.

To gain further insight into the performance of GEMS near cavitation bubbles, we used a potential flow model to investigate the coalescence of the entrapped gas in neighboring microcavities. Our simulations begin with a cavitation bubble of initial radius $R_0 = 200$ μm at 1300 bar. Next, we vary the inter-cavity distance and the location of the cavitation bubble's inception from the surface in the range of 800 to 4000 μm (Fig. 8). To simulate the coalescence of entrapped gas from neighboring microcavities, we use the following criterion: If the overlapping volume of gas in adjacent cavities exceeds that of a microcavity itself, the coalescence takes place. Thermodynamically, the change in the energy of the liquid-vapor interface is higher than the work required to overcome the pinning forces at the solid-liquid-vapor interface.

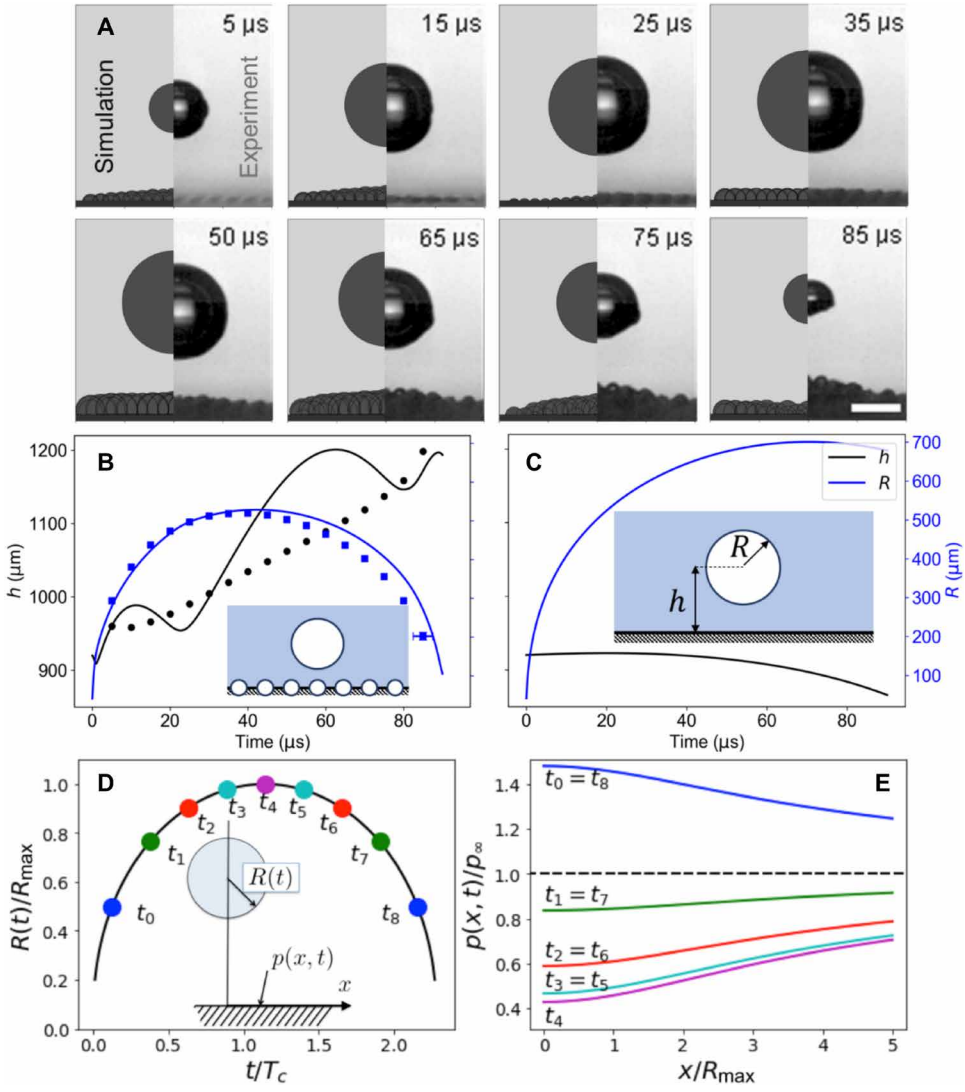

Fig. 7. Comparison between the experimental and simulated results. (**A**) Selected frames of the bubble dynamics. The left half of each frame depicts a simulated result, and the right half is the experimental result from the high-speed images captured. Scale bar, 500 μm. The inset numbers on all the panels refer to time in microseconds after the generation of the cavitation bubble. (**B** and **C**) Time series results derived from the numerical simulation and experimental results as shown in Fig. 5. Panel (B) shows the bubble collapsing near a microcavity substrate. The scatter blue data points represent experimental results, and the continuous blue line denotes simulated values. Error bars are equal for each point, and only the error bars of the last data points are shown for better visualization. The scatter black data points represent the position of the bubble's centroid, while the continuous black line portrays the position of the simulated bubble's centroid. Panel (C) shows results of a bubble collapsing near a smooth surface. The blue and black lines are the bubble's radius and the location of the bubble's centroid, respectively. (**D**) Simulated radial dynamics of a bubble collapsing near a solid surface. (**E**) Resulting pressure field on the surface $p(x,t)$. Photo credit: Silvestre Roberto Gonzalez-Avila, OVGU.

Figure 8 displays the region where coalescence is expected, which compromises the integrity of the present GEMS design. For the smaller inter-cavity distances, 210 to 260 μm, the entrapped gas in adjacent cavities coalesces even when the nucleation bubbles are created as far as corresponding to the standoff parameter of $\gamma \sim 5$. With larger inter-cavity distances, microcavities can withstand nucleation events closer to the surface. Yet, when $\gamma < 2$, coalescence events take place at all the inter-cavity distances calculated. In the experiments, with inter-cavity distance of 212 μm, we started to observe coalescence for $\gamma \sim 2.2$. At $\gamma \sim 3.0$, the entrapped gas protrudes out of the cavities, comes into contact, but does not merge. The liquid film between them is not completely drained; hence, coalescence does not occur. This feature cannot be captured by the potential flow model. The model only provides a conservative estimate of the occurrence of coalescence and is too simple to simulate the complex flow near the microcavities. Nevertheless, the results presented here provide an initial design guidance that can motivate future experimental and numerical studies.

DISCUSSION

Here, we report on a biomimetic coating-free approach for mitigating cavitation erosion. In this study, the mushroom-shaped features found in the hairs and cuticles of sea skaters and springtails, respectively, are carved onto SiO_2/Si substrates using microfabrication techniques. The experiments demonstrate that the resulting surfaces,

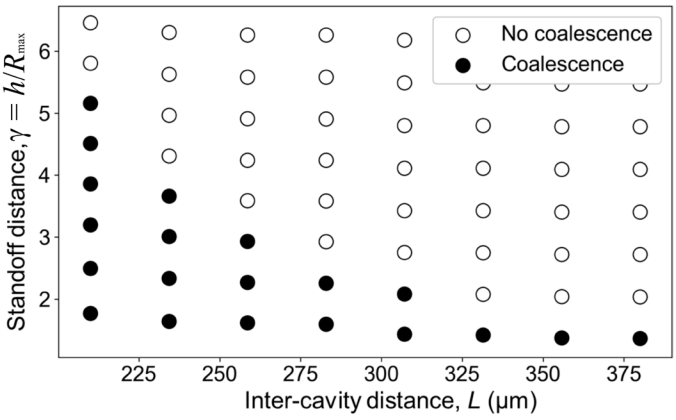

Fig. 8. Parametric plot built from the numerical results of the model showing the region where coalescence of the entrapped gas in adjacent microcavities is expected to take place.

silica-GEMS, can robustly trap air while under water, with or without hydrophobic coatings. Next, the response of the trapped air in silica-GEMS to laser-induced cavitation bubbles was investigated with high-speed imaging. The movies show that silica-GEMS repel the liquid jets produced by the collapse of bubbles at distances above $\gamma = 5.1$. For $3.0 \leq \gamma \leq 5.1$, the trapped air in the silica-GEMS is stable up for 30 cycles, where the laser-induced bubbles were repelled without "deactivation" of the silica-GEMS, i.e., the liquid only partially intruded inside the cavities. For $1.2 < \gamma < 3.0$, this number reduces from one to five cycles before the silica-GEMS is deactivated entirely. The performance of silica-GEMS is indistinguishable from that of perfluorinated GEMS for the same tests and conditions. We test the absolute limits of our surfaces before their instant deactivation by nucleating bubbles at much closer distances to silica-GEMS, such as $\gamma = 0.7$ and $R_{max} = 430$ μm. At these short distances, the entrapped gas can still dampen the collapse of cavitation bubbles, but the trapped air coalesces with the bubbles, and thus, the system is deactivated. The functionality of the silica-GEMS is due to the low-pressure fields induced by the cavitation bubbles, which causes the gas trapped inside silica-GEMS to protrude and act as a free boundary that repels the liquid jet. A simple potential flow model was used to verify this hypothesis, which qualitatively reproduces the repellence of the cavitation bubble from silica-GEMS.

Additional work is needed to address certain design challenges such as resupplying gas to the microcavities after deactivation, which is an ongoing area of research (*48*, *49*). For instance, cavitation bubbles themselves may provide the necessary pull force for refilling from a gas reservoir connected to the back of the substrate. A promising approach is the use of self-recovery substrates recently studied theoretically by Lisi *et al.* (*50*). The short recovery time scale of optimized textured surfaces, in principle, might allow the use of micropatterned surfaces in real-world applications. Another strategy to explore is the decrease of the microcavities' diameter to increase the liquid entry pressure for GEMS to enhance the robustness of the air entrapment. However, for long-term applications, this measure might be counterproductive due to the capillary condensation of water. This method may be suitable for low vapor pressure liquids such as hexadecane and mineral oils. Yet, the properties of microtextures still need to be optimized, such as size (diameter and depth), shape (circular or noncircular), profile (reentrant and doubly reentrant), and distribution (inter-cavity distance and lattice), and further detailed investigations are required under realistic cavitation conditions on the role of different liquid properties, such as viscosity and vapor pressure (*32*). In hydrodynamic cavitation, adding gas pockets (i.e., the entrapped gas inside GEMS) to the structure may result in adding cavitation nuclei and therefore might worsen the situation rather than mitigate erosion. While no answer to this threat is possible without careful experiments, the location where the GEMS structure is placed may affect its function. An example would be a hydrofoil that can potentially be damaged by a bubble cloud collapse (*2*). In this case, if the GEMS structure is placed downstream the hydrofoil, near the location of the collapse, the cloud may be repelled or at least fed with some noncondensable gas to dampen the collapse.

Next, we note that the experiments reported in this study comprised deionized water that was in thermodynamic equilibrium with air. If an application involves the use of degassed water, such as in the oil and gas sector (*51*), the air entrapped in the GEMS might be lost quickly over time, depending on the solubility of the gas in the liquid and diffusivity (*52*). We note that even superhydrophobic surfaces will lose the entrapped air in such a scenario, transitioning to the Wenzel state, but an in-depth investigation is beyond the scope of this report. It must be recognized that the choice of SiO_2/Si wafers as the model system and the use of integrated circuit microfabrication techniques are limited to a proof-of-concept demonstration only. Scalable platforms for translating GEMS microtexture onto common materials should be explored. For instance, new ways of realizing arrays of mushroom-shaped pillars are being explored, such as microelectric discharge machining of steel (*21*), microfluidic emulsion templating of polyvinyl alcohol (*23*), and injection molding of polypropylene (*53*); these methods could be modified for achieving GEMS. The realization of the first-ever membranes for desalination (by direct contact membrane distillation) derived from hydrophilic polymethylmethacrylate sheets using computer numerical control drilling and CO_2 laser (*54*) is another promising development. To conclude, the experiments and numerical models demonstrate that the silica-GEMS design presents an effective means to counteract the negative effects of cavitation erosion, and our findings advance the rational design of materials and processes to mitigate and prevent cavitation erosion.

MATERIALS AND METHODS

Fabrication of the silica-GEMS

The microfabrication procedure for silica-GEMS has been reported previously (*24*, *32*, *33*). Please refer to section S1 and fig. S1 for the main steps. Some of the silica-GEMS were covalently grafted with FDTS using the Molecular Vapor Deposition (MVD) 100E System. Before MVD processing, we exposed the surfaces to a 100-W O_2 plasma for 5 min. Please see section S2 and fig. S2 for more details.

Characterization of wettability and entrapment of air in GEMS

The static and advancing/receding contact angle measurements (water) were performed in a KRÜSS drop shape analyzer (DSA100) at a rate of 0.2 μl s^{-1}. We used the "Advance" software for the analysis of the contact angles of the observed drops. All data points were averaged from at least five measurements.

For scanning electron microscopy (SEM; FEI Quanta 600) analysis, the samples were cleaved using a diamond tip scriber and coated with a 4-nm Au/Pd alloy layer to minimize electrical charging.

To visualize the entrapment of gas inside the silica-GEMS underwater, we added Rhodamine B to the liquid and used a confocal laser-scanning microscope (Zeiss LSM 710; fig. S5). Sequential images (1024 pixels × 1024 pixels) were taken in the *Z*-stack mode, from the bottom of the cavities up to 50 μm above the solid surface, using the laser power 0.3 mW. Three-dimensional rendering of those images and sectioning of the liquid-vapor interface to aid visualization were achieved using the Imaris v.8.1 software.

Cavitation experimental setup

We performed the tests in an acrylic cuvette filled with deionized water, in which the silica-GEMS was attached to one of the walls, as shown in Fig. 2 and fig. S6. The bubble was generated by triggering a single pulse from a laser (wavelength of 532 nm, Q-switched Nd:YAG laser with pulse duration of 6 ns and pulse energy of approximately 1 mJ) focused on specific locations near the surface. We used two high-speed cameras to record the cavitation events. A high-speed camera (Photron FASTCAM SA1.1) captured the side view (see Fig. 5B), equipped with a 60-mm macro lens (Nikon) at full magnification (resolution of 20 μm per pixel). A Revox LED fiber optic lamp (SLG-150V) was used to provide back illumination with mildly diffused light. The top-view camera (Photron Fastcam SA-X2) was coupled with an MP-E 65-mm Canon lens set at ×2 magnification to obtain a resolution of 10 μm per pixel, as depicted in Fig. 5C. The lens observed the front-illuminated scene from the same illumination source as a double light guide (Sumita AAAR-007W, 1.5 in length) was used. Framing rates were 200,000 frames s^{-1} except for Fig. 5B, which was captured at 40 kfps. A pulse delay generator (Berkeley Scientific, BNC model 575) triggered and synchronized the laser and the two high-speed cameras.

Numerical simulation

We simulated silica-GEMS as a set of multiple gas bubbles, where each bubble represents entrapped gas in one cavity. In addition, we added two more sources term, one for the cavitation bubble and another for its mirror image across the boundary, to complete the potential flow problem. The simulations neglect viscosity and the compressibility of liquid, as well as coalescence events of the expanding gas bubbles. The state of a bubble i is defined by two variables: its instantaneous radius R_i and its position $\mathbf{x}_i$, which are solved with two equations. The first equation models the change of the bubble's momentum because of the acting forces, e.g., the Bjerknes force and the drag force in Eq. 1. The second equation describes the bubble's expansion and collapse driven by its internal pressure, ambient pressure, and pressure induced by other bubbles. For this, we use the Keller-Miksis equation

$$\left(1-\frac{\dot{R}_i}{c}\right)R_i\ddot{R}_i+\left(\frac{3}{2}-\frac{\dot{R}_i}{2c}\right)\dot{R}_i^2=\frac{1}{\rho}\left(1+\frac{\dot{R}_i}{c}\right)(p_l-p_\infty)+\frac{R_i}{\rho c}\frac{d}{dt}p_l-\frac{1}{\rho}p_i \quad (2)$$

where c is the speed of sound, p_l is the liquid pressure at the bubble wall, and p_i is the pressure field induced by neighboring bubbles. Section S6 provides details on the geometry and the solution procedure of the coupled equations.

SUPPLEMENTARY MATERIALS

Supplementary material for this article is available at http://advances.sciencemag.org/cgi/content/full/6/13/eaax6192/DC1

Section S1. Microfabrication process of silica-GEMS
Section S2. MVD of FDTS on silica surfaces
Section S3. The Cassie-Baxter model
Section S4. Experimental setup
Section S5. Bubble dynamics close to GEMS coated with FDTS
Section S6. Details on the numerical simulation
Section S7. Movies
Fig. S1. Schematic of the microfabrication process of silica-GEMS.
Fig. S2. Schematic of the FDTS deposited onto silica-GEMS.
Fig. S3. Schematic representation of silica-GEMS with mushroom-shaped cavities.
Fig. S4. Schematic representation of meniscus displacement if an external pressure is applied onto the liquid or if the trapped air is lost by dissolution in water.
Fig. S5. Schematic illustration of the laser confocal microscope experiment.
Fig. S6. Schematic diagram of the bubble cavitation test section.
Fig. S7. Bubble dynamics of a cavitation bubble next to FDTS-coated silica-GEMS.
Fig. S8. FDTS-coated silica-GEMS.
Fig. S9. Selected frames of a cavitation bubble created near partially filled microcavities.
Fig. S10. Selected frames of microcavity deactivation for different γ values.
Fig. S11. Schematic representation of the geometry of the numerical simulation.
Table S1. Table listing the major design parameters for the cavities depicted in fig. S3.
Table S2. A summary of contact angle with all samples presented in this work: (θ_o) intrinsic contact angles, (θ_r) apparent contact angles, (θ_A) advancing contact angles, (θ_R) receding contact angles, and (θ_{Pr}) predicted contact angles, for water droplets.
Movie S1. Bubble dynamics near a glass substrate, $\gamma = 4.8$, $R_{max} = 630$ μm.
Movie S2. Side view of bubble dynamics beside an uncoated GEMS, $\gamma = 5.1$, $R_{max} = 610$ μm.
Movie S3. Front view of bubble dynamics on uncoated GEMS, $\gamma = 5.1$, $R_{max} = 610$ μm.
Movie S4. Side view of bubble dynamics on coated GEMS, $\gamma = 4.7$, $R_{max} = 600$ μm.
Movie S5. Front view of bubble dynamics on coated GEMS, $\gamma = 4.7$, $R_{max} = 600$ μm.
Movie S6. Bubble dynamics on uncoated GEMS, $\gamma = 1.8$, $R_{max} = 530$ μm.
Movie S7. Bubble dynamics on coated GEMS, $\gamma = 1.7$, $R_{max} = 520$ μm.
Movie S8. Bubble dynamics on uncoated GEMS, $\gamma = 0.7$, $R_{max} = 430$ μm.
Movie S9. Bubble dynamics on coated GEMS, $\gamma = 0.7$, $R_{max} = 470$ μm.
Movie S10. Bubble dynamics on a noncoated GEMS with filled and partially filled microcavities, $\gamma = 2.1$, $R_{max} = 430$ μm.

REFERENCES AND NOTES

1. J. R. Blake, D. Gibson, Cavitation bubbles near boundaries. *Annu. Rev. Fluid Mech.* **19**, 99–123 (1987).
2. C. E. Brennen, *Cavitation and Bubble Dynamics* (Cambridge Univ. Press, 2013).
3. K.-H. Kim, G. Chahine, J.-P. Franc, A. Karimi, *Advanced Experimental and Numerical Techniques for Cavitation Erosion Prediction* (Springer, 2014), vol. 106.
4. A. Philipp, W. Lauterborn, Cavitation erosion by single laser-produced bubbles. *J. Fluid Mech.* **361**, 75–116 (1998).
5. J. R. Haines, B. W. Riemer, D. K. Felde, J. D. Hunn, S. J. Pawel, C. C. Tsai, Summary of cavitation erosion investigations for the SNS mercury target. *J. Nucl. Mater.* **343**, 58–69 (2005).
6. D. A. McClintock, B. Riemer, P. D. Ferguson, A. J. Carroll, M. J. Dayton, Initial observations of cavitation-induced erosion of liquid metal spallation target vessels at the Spallation Neutron Source. *J. Nucl. Mater.* **431**, 147–159 (2012).
7. G. Bark, R. E. Bensow, Hydrodynamic mechanisms controlling cavitation erosion. *Int. Shipbuild. Prog.* **60**, 345–374 (2013).
8. F. T. Cheng, C. T. Kwok, H. C. Man, Laser surfacing of S31603 stainless steel with engineering ceramics for cavitation erosion resistance. *Surf. Coat. Technol.* **139**, 14–24 (2001).
9. R. J. Wood, Tribo-corrosion of coatings: A review. *J. Phys. D Appl. Phys.* **40**, 5502 (2007).
10. R. Singh, S. K. Tiwari, S. K. Mishra, Cavitation erosion in hydraulic turbine components and mitigation by coatings: Current status and future needs. *J. Mater. Eng. Perform.* **21**, 1539–1551 (2012).
11. P. B. Robinson, J. R. Blake, T. Kodama, A. Shima, Y. Tomita, Interaction of cavitation bubbles with a free surface. *J. Appl. Phys.* **89**, 8225–8237 (2001).
12. T. Verho, C. Bower, P. Andrew, S. Franssila, O. Ikkala, R. H. Ras, Mechanically durable superhydrophobic surfaces. *Adv. Mater.* **23**, 673–678 (2011).
13. H. Mishra, A. M. Schrader, D. W. Lee, A. G. Jr., S.-Y. Chen, Y. Kaufman, S. Das, J. N. Israelachvili, Time-dependent wetting behavior of PDMS surfaces with bioinspired hierarchical structures. *ACS Appl. Mater. Interfaces* **8**, 8168–8174 (2016).
14. N. Subramanian, A. Qamar, A. Alsaadi, A. G. Jr, M. G. Ridwan, J.-G. Lee, S. Pillai, S. Arunachalam, D. Anjum, F. Sharipov, N. Ghaffour, H. Mishra, Evaluating the potential

of superhydrophobic nanoporous alumina membranes for direct contact membrane distillation. *J. Colloid Interface Sci.* **533**, 723–732 (2019).
15. M. Rezaei, D. M. Warsinger, J. H. Lienhard V, M. C. Duke, T. Matsuura, W. M. Samhaber, Wetting phenomena in membrane distillation: Mechanisms, reversal, and prevention. *Water Res.* **139**, 329–352 (2018).
16. A. B. Lindstrom, M. J. Strynar, E. L. Libelo, Polyfluorinated compounds: Past, present, and future. *Environ. Sci. Technol.* **45**, 7954–7961 (2011).
17. R. Hensel, C. Neinhuis, C. Werner, The springtail cuticle as a blueprint for omniphobic surfaces. *Chem. Soc. Rev.* **45**, 323–341 (2016).
18. L. Cheng, Biology of Halobates (Heteroptera: Gerridae). *Annu. Rev. Entomol.* **30**, 111–135 (1985).
19. J. Nickerl, R. Helbig, H.-J. Schulz, C. Werner, C. Neinhuis, Diversity and potential correlations to the function of Collembola cuticle structures. *Zoomorphology* **132**, 183–195 (2013).
20. L. Cheng, Marine and freshwater skaters: Differences in surface fine structures. *Nature* **242**, 132 (1973).
21. P. B. Weisensee, E. J. Torrealba, M. Raleigh, A. M. Jacobi, W. P. King, Hydrophobic and oleophobic re-entrant steel microstructures fabricated using micro electrical discharge machining. *J. Micromech. Microeng.* **24**, 095020 (2014).
22. S. Arunachalam, E. M. Domingues, R. Das, J. Nauruzbayeva, U. Buttner, A. Syed, H. Mishra, Rendering SiO2/Si Surfaces Omniphobic by Carving Gas-Entrapping Microtextures Comprising Reentrant and Doubly Reentrant Cavities or Pillars. *J. Vis. Exp.* **156**, e60403 (2020).
23. P. Zhu, T. Kong, X. Tang, L. Wang, Well-defined porous membranes for robust omniphobic surfaces via microfluidic emulsion templating. *Nat. Commun.* **8**, 15823 (2017).
24. E. M. Domingues, S. Arunachalam, H. Mishra, Doubly reentrant cavities prevent catastrophic wetting transitions on intrinsically wetting surfaces. *ACS Appl. Mater. Interfaces* **9**, 21532–21538 (2017).
25. D. Seo, A. M. Schrader, S.-Y. Chen, Y. Kaufman, T. R. Cristiani, S. H. Page, P. H. Koenig, Y. Gizaw, D. W. Lee, J. N. Israelachvili, Rates of cavity filling by liquids. *Proc. Natl. Acad. Sci. U.S.A.* **115**, 8070–8075 (2018).
26. R. Hensel, A. Finn, R. Helbig, H.-G. Braun, C. Neinhuis, W.-J. Fischer, C. Werner, Biologically inspired omniphobic surfaces by reverse imprint lithography. *Adv. Mater.* **26**, 2029–2033 (2014).
27. R. Hensel, R. Helbig, S. Aland, H.-G. Braun, A. Voigt, C. Neinhuis, C. Werner, Wetting resistance at its topographical limit: The benefit of mushroom and serif T structures. *Langmuir* **29**, 1100–1112 (2013).
28. R. Das, S. Arunachalam, Z. Ahmad, E. Manalastas, A. Syed, U. Buttner, H. Mishra, Proof-of-Concept for Gas-Entrapping Membranes Derived from Water-Loving SiO 2/Si/SiO 2 Wafers for Greener Desalination. *J. Vis. Exp.* **157**, e60583 (2020).
29. R. N. Wenzel, Resistance of solid surface to wetting by water. *Ind. Eng. Chem.* **28**, 7 (1936).
30. A. B. D. Cassie, S. Baxter, Wettability of porous surfaces. *Trans. Faraday Soc.* **40**, 0546–0550 (1944).
31. Y. Kaufman, S.-Y. Chen, H. Mishra, A. M. Schrader, D. W. Lee, S. Das, S. H. Donaldson Jr., J. N. Israelachvili, Simple-to-apply wetting model to predict thermodynamically stable and metastable contact angles on textured/rough/patterned surfaces. *J. Phys. Chem. C* **121**, 5642–5656 (2017).
32. E. M. Domingues, S. Arunachalam, J. Nauruzbayeva, H. Mishra, Biomimetic coating-free surfaces for long-term entrapment of air under wetting liquids. *Nat. Commun.* **9**, 3606 (2018).
33. S. Arunachalam, R. Das, J. Nauruzbayeva, E. M. Domingues, H. Mishra, Assessing omniphobicity by immersion. *J. Colloid Interface Sci.* **534**, 156–162 (2019).
34. N. Bremond, M. Arora, C.-D. Ohl, D. Lohse, Controlled multibubble surface cavitation. *Phys. Rev. Lett.* **96**, 224501 (2006).
35. R. Mettin, I. Akhatov, U. Parlitz, C. D. Ohl, W. Lauterborn, Bjerknes forces between small cavitation bubbles in a strong acoustic field. *Phys. Rev. E* **56**, 2924 (1997).
36. S. R. Gonzalez Avila, C.-D. Ohl, Fragmentation of acoustically levitating droplets by laser-induced cavitation bubbles. *J. Fluid Mech.* **805**, 551–576 (2016).
37. J. S. Rowlinson, B. Widom, *Molecular Theory of Capillarity* (Dover Publication, 2002).
38. W. Chen, W. Chen, A. Y. Fadeev, M. C. Hsieh, D. Öner, J. Youngblood, T. J. McCarthy, Ultrahydrophobic and ultralyophobic surfaces: Some comments and examples. *Langmuir* **15**, 3395–3399 (1999).
39. R. Dufour, M. Harnois, V. Thomy, R. Boukherroub, V. Senez, Contact angle hysteresis origins: Investigation on super-omniphobic surfaces. *Soft Matter* **7**, 9380–9387 (2011).
40. W. Lauterborn, C. Lechner, M. Koch, R. Mettin, Bubble models and real bubbles: Rayleigh and energy-deposit cases in a Tait-compressible liquid. *IMA J. Appl. Math.* **83**, 556–589 (2018).
41. O. Supponen, D. Obreschkow, M. Tinguely, P. Kobel, N. Dorsaz, M. Farhat, Scaling laws for jets of single cavitation bubbles. *J. Fluid Mech.* **802**, 263–293 (2016).
42. A. Vogel, W. Lauterborn, Acoustic transient generation by laser-produced cavitation bubbles near solid boundaries. *J. Acoust. Soc. Am.* **84**, 719–731 (1988).
43. B. M. Borkent, S. Gekle, A. Prosperetti, D. Lohse, Nucleation threshold and deactivation mechanisms of nanoscopic cavitation nuclei. *Phys. Fluids* **21**, 102003 (2009).
44. A. Zijlstra, D. F. Rivas, H. J. G. E. Gardeniers, M. Versluis, D. Lohse, Enhancing acoustic cavitation using artificial crevice bubbles. *Ultrasonics* **56**, 512–523 (2015).
45. D. F. Rivas, J. Betjes, B. Verhaagen, W. Bouwhuis, T. C. Bor, D. Lohse, J. G. E. Gardeniers, Erosion evolution in mono-crystalline silicon surfaces caused by acoustic cavitation bubbles. *J. Appl. Phys.* **113**, 064902 (2013).
46. R. Mettin, S. Luther, C.-D. Ohl, W. Lauterborn, Acoustic cavitation structures and simulations by a particle model. *Ultrason. Sonochem.* **6**, 25–29 (1999).
47. L. Rayleigh, VIII. On the pressure developed in a liquid during the collapse of a spherical cavity. *Lond. Edinb. Dubl. Phil. Mag. J. Sci.* **34**, 94–98 (1917).
48. C. Lee, C.-J. Kim, Underwater restoration and retention of gases on superhydrophobic surfaces for drag reduction. *Phys. Rev. Lett.* **106**, 220401 (2011).
49. Y. Xue, P. Lv, H. Lin, H. L. Duan, Underwater superhydrophobicity: Stability, design and regulation, and applications. *Appl. Mech. Rev.* **68**, 030803 (2016).
50. E. Lisi, M. Amabili, S. Meloni, A. Giacomello, C. M. Casciola, Self-recovery superhydrophobic surfaces: Modular design. *ACS Nano* **12**, 359–367 (2018).
51. M. P. Yutkin, H. Mishra, T. W. Patzek, J. Lee, C. J. Radke, Bulk and surface aqueous speciation of calcite: Implications for low-salinity waterflooding of carbonate reservoirs. *SPE J.* **23**, 84–101 (2018).
52. M. M. Benjamin, *Water Chemistry* (Waveland Press Inc., ed. 2, 2015).
53. K. Mielonen, T. A. Pakkanen, Superhydrophobic hierarchical three-level structures on 3D polypropylene surfaces. *J. Micromech. Microeng.* **29**, 025006 (2019).
54. R. Das, S. Arunachalam, Z. Ahmad, E. Manalastas, H. Mishra, Bio-inspired gas-entrapping membranes (GEMs) derived from common water-wet materials for green desalination. *J. Membr. Sci.* **588**, 117185 (2019).

Acknowledgments: We thank X. Pita, scientific illustrator at King Abdullah University of Science and Technology (KAUST), for preparing Fig. 2 and V. Unkefer (KAUST) for assistance in editing of the manuscript. H.M. and S.A. thank G. Mahadik (KAUST) for providing specimens of sea skaters (*H. germanus*) and W. S. Hwang (National University of Singapore) and L. Cheng (Scripps Institution of Oceanography, USA) for providing specimens of springtails. **Funding:** The research reported in this publication was supported by funding from KAUST under award number BAS/1/1070-01-01. **Author contributions:** H.M., C.-D.O., and S.R.G.-A. conceived the experiment. H.M. conceived the micropatterned surfaces. S.A. and E.M.D. fabricated the micropatterned surfaces. S.R.G.-A. designed the experimental setup. D.M.N. performed the numerical simulations with contributions and input from C.-D.O. and S.R.G.-A. D.M.N. performed the experiments and the data analysis with contributions and inputs from all authors. All authors contributed to the writing of the manuscript. **Competing interests:** S.R.G.-A., D.M.N., H.M., and C.-D.O. are inventors on a patent application related to this work, "Surface protection against cavitation erosion" (European Patent Application EP 0752-5518 from 7 March 2019). The authors declare no other competing interests. **Data and materials availability:** All data needed to evaluate the conclusions in the paper are present in the paper and/or the Supplementary Materials. Additional data related to this paper may be requested from the authors.

Submitted 8 April 2019
Accepted 31 December 2019
Published 27 March 2020
10.1126/sciadv.aax6192

Citation: S. R. Gonzalez-Avila, D. M. Nguyen, S. Arunachalam, E. M. Domingues, H. Mishra, C.-D. Ohl, Mitigating cavitation erosion using biomimetic gas-entrapping microtextured surfaces (GEMS). *Sci. Adv.* **6**, eaax6192 (2020).

Science Advances

Mitigating cavitation erosion using biomimetic gas-entrapping microtextured surfaces (GEMS)

Silvestre Roberto Gonzalez-Avila, Dang Minh Nguyen, Sankara Arunachalam, Eddy M. Domingues, Himanshu Mishra and Claus-Dieter Ohl

Sci Adv **6** (13), eaax6192.
DOI: 10.1126/sciadv.aax6192